Applied Catalysis B: Environmental 324 (2023) 122189

Contents lists available at ScienceDirect

Applied Catalysis B: Environmental

journal homepage: www.elsevier.com/locate/apcatb

High performance of conversion and selectivity of methane to CO via Pt-Pd core-shell structural catalyst

Haojie Geng [a,b,*], Haobo Zhao [a], Siyu Yu [a], Dongwei Li [a,c], Hong Lei [a,c], Yuting Zhang [a]

[a] School of Chemistry and Chemical Engineering, Southwest University, Chongqing 400715, China
[b] Chongqing Key Laboratory of Soft-Matter Material Chemistry and Function Manufacturing, Southwest University, Chongqing 400715, China
[c] Chongqing University of Education, Chongqing 400065, China

ARTICLE INFO

Keywords:
Pt-core@Pd-shell catalyst
Methane activation
Surface oxygen concentration
Vacancy
Coordination

ABSTRACT

Catalytic oxidation of methane to CO has been investigated in this paper with the employment of a novel core shell structural Pt-Pd catalyst, which exhibits high performance in conversion and selectivity. To figure out the correlation of surface species to reaction selectivity, the particle structure, reaction intermediates, etc. have been characterized via reaction kinetics, isotopic exchange, TPR, and various "in situ" techniques, such as FTIR, XPS and XAS. The oxygen concentration, vacancy, metal surface sites, coordination number, etc. have been further calculated. Core shell catalyst attends to form strong bonding / coordination with carbon ions, therefore, it is very active to dissociate C-H bond in methane. The strong combination of the low coordinated Pd sites to surface oxygen (O*) leads to the blockage or reduction of the complete oxidation of CO, resulting in good catalytic performance of the core shell structural Pt-Pd catalyst in methane conversion and CO selectivity.

1. Introduction

The catalytic oxidation of methane to C1 or C2 chemical products is a promising way to achieve high efficient utilization and low emission of carbon [1–3]. The partial oxidation of methane using weak oxidant, which leads to the synthesis of high value added products such as CO, CH_3OH, or HCOOH instead of CO_2, has drawn much attention recently [4,5]. However, this methodology still suffers from low methane conversion and low selectivity towards desired products under relatively mild conditions, and complex procedures required to separate the obtained gaseous products to achieve high purity of the desired products [6–8].

Methane activation is kinetically challenging, because its C-H bond exhibits the highest binding energy among all hydrocarbons (440 kJ/mol). Effective catalysts, typically transition metals, possess formidable coordinated ability to stabilize the activated transition state of C-H bond. The catalytic performance of different exposed active sites with varied position and property is actually different. For example, surface sites located at the edge or corner are known to possess higher free energy and coordination ability, and thus high catalytic performance [9–11].

Pd and Pt are the most frequently applied catalysts for partial oxidation of methane. The exposed Pt atoms possess strong coordination performance in C-H bond activation, while Pd species need oxygen assistance to complete this activation [12–16]. Under certain reaction conditions, the surface oxygen concentration is positively correlated to methane conversion. Dissociated methane molecules are combined with oxygen species, forming CO* intermediates adsorbed onto the catalyst surface. With the presence of a large number of vacancies around the intermediates, the further oxidation of CO would be blocked, and CO would be released to atmosphere as the product [17,18]. Therefore, the regulation of surface chemical environment, such as reactant concentration, energy, coordination, etc. is highly important to achieve high CO selectivity [19–21].

Pt-Pd alloy shows high catalytic activity for C-H bond activation. Although Pt-Pd alloy provides both Pd and Pt active sites to catalytic reaction, the fully oxidation of methane is mainly performed over exposed Pt sites. To reduce or remove surface Pt sites, one approach is to establish a plane with single species by developing novel structures such as core shell structure, coating structure, etc., synthesized by means of chemical deposition or ion exchange. Among them, with the synthesis of core shell structure, the electronic structure of the exposed sites can be altered to change the binding energy of surface species, and as a result to control the formed products [22,23].

* Corresponding author at: School of Chemistry and Chemical Engineering, Southwest University, Chongqing 400715, China.
E-mail address: hjgeng@swu.edu.cn (H. Geng).

https://doi.org/10.1016/j.apcatb.2022.122189
Received 17 July 2022; Received in revised form 10 November 2022; Accepted 15 November 2022
Available online 23 November 2022

Reaction intermediates affect the formation of products. For example, more surface vacancy leads to increased CO selectivity, but decreased methane conversion, resulting in a lower CO productivity [24,25]. One effective way to solve this problem is the intensification of the combination between exposed active site and surface oxygen, where these surface oxygen species is not easy to be reduced. This strong combination may limit further oxidation of CO [26–29]. Whereas for CH_x free radicals generated from methane dissociation, they could directly react with these oxygen species due to strong coordination and reduction behavior [30–32]. In general, the variation in binding ability of surface active sites requires the design of novel catalyst structures, such as core shell structural catalyst or single atom catalyst. These structures are beneficial for the improvement of the surface chemical environment that increases the surface energy, coordination, etc., and the reactivity of surface sites [33–36].

In this work, a novelty core shell structural catalyst has been designed and synthesized, aiming to enhance the C-H bond activation ability of the catalyst and block CO complete oxidation in oxidative environment. The surface chemical environment of Pd species, especially the intermediates and coordination, have been tuned to achieve high conversion and selectivity of methane oxidation. The variation of oxygen concentration, vacancy, coordination number of Pd-O pair under reaction conditions have been characterized and analyzed using "in situ" techniques (e.g., FTIR, XPS and XAS), isotopic exchange, reaction kinetics, and TPR, etc. It was found that oxygen concentration is positively correlated to methane conversion, while increased amount of uncovered sites or vacancies leads to increased CO selectivity. A low coordination number of Pd-O bond is beneficial for intensifying its binding energy, hindering the complete oxidation of CO. This research provides a new idea for catalyst design for methane direct oxidation.

2. Experiment

2.1. Synthesis of core shell structural bimetallic catalyst

SiC nanomaterials were synthesized by direct magnesiothermic reduction [37–39] of SiO_2/C composites at temperature of 700 ℃ and applied as the support. The total reduction reaction can be depicted as $C + SiO_2 + Mg \rightarrow SiC + MgO$. Its specific surface area and pore volume were measured via BET technique (N_2 adsorption) to be 125 m^2/g and 0.88 cm^3/g, respectively. Pd and Pt species were loaded over SiC surface by impregnation of the mixed solution of $Pd(NO_3)_2$ (Sigma Aldrich, 99.999%) and $Pt(NH_3)_4(NO_3)_2$ (Sigma Aldrich, 99.999%) for 12 h. The mass loading of Pd species was fixed to be 1 wt%, while the Pt mass loading was varied from 0.275 *wt.*% to 3.67 *wt.*%, in other words, the Pt: Pd ratio was in the range of 0.15–2. After impregnation, all the catalysts were dried at 120 ℃ in air for 2 h, and then calcined in flow air at 400–450 ℃ with heating rate of 2 ℃/min and a flow rate of 50 mL/min. Detailed parameters are shown in Table 1.

Core shell structural catalysts were then synthesized from the above obtained Pd-Pt alloy nanoparticles (NPs) with the employment of O_3 induced segregation, similar as that reported in literature [40]. The used O_3 pulse system was schematically shown in Fig. S1. After reduction of Pd-Pt alloy in hydrogen (2 *vol.*% H_2, Ar balance) for 5 h, the system was degassed for 2 h at 700 ℃ to remove chemisorbed species. Subsequently, O_3 pulses were introduced to catalyst bed, which released highly active oxygen adatoms (O*) that chemisorbed on nanoparticle surface. It is known that the surface free energy of oxidized Pd (0.53 J/m^2) is much lower than that of Pt species (2.48 J/m^2) (Table S2). Hence, the thermodynamic instable Pt atoms with higher free energy were migrated from surface to the inner core to coordinate with more atoms to lower their free energy. This migration led to the formation of core shell structural catalysts. The detailed procedure for the synthesis of Pt (core) - Pd (shell) catalysts is shown in Supplementary Information S1. As for monometallic Pd or Pt samples, they were only reduced with hydrogen (2 *vol.*% H_2, Ar balance) for 5 h and then treated in chemisorption system by using oxygen or hydrogen as the probe molecules to measure their dispersion, respectively.

Table 1 provides the treatment parameters and properties (e.g., treatment temperature, particle dispersion, and average particle diameter) of different catalysts including monometallic Pd, monometallic Pt and bimetallic Pd-Pt catalysts. Generally, larger particle diameters were obtained with higher reduction and/or calcination temperature.

2.2. Assessment of conversion, selectivity and intrinsic kinetics for methane oxidation

The catalytic performance of synthesized catalysts for partial oxidation of methane was evaluated in a fixed bed reactor (quartz tube, ~8 mm diameter), in which reactant gas was controlled by mass flow controller (HORIBA, FMA-A4000, 0 ~ 100 mL/min). The temperature was measured by a k-type thermocouple located in the center of the reactor. Here, 1 g catalyst was loaded into the quartz tube reactor with a dilution ratio of 1:10 ($m_{PdPt/SiC}$: m_{SiC}). The total flow rate (CH_4, O_2, balance gas, etc.) was kept at 100 mL/min, and the space velocity was controlled to be 6×10^3 $cm^3/(g_{cat} \bullet h)$. At the outlet of the reactor, the exhaust gas was linked directly to an online GC (Agilent, 7600 A) that was equipped with a methanator and a FID detector. This GC was able to measure carbon-based molecules, such as CH_4, CO_2, CO, etc., from 5 ppm to 5000 ppm. The results were collected every three minutes. Catalytic conversion (x_{CH_4}) and selectivity (S_{CO}, S_{CO_2}) of methane catalytic reaction were defined as follows:

$$x_{CH_4} = \frac{F_{CH_4,in} - F_{CH_4,out}}{F_{CH_4,in}} \times 100\% \quad (1)$$

$$S_{CO} = \frac{F_{CO,out}}{F_{CH_4,in} - F_{CH_4,out}} \times 100\% \quad (2)$$

$$S_{CO_2} = \frac{F_{CO_2,out}}{F_{CH_4,in} - F_{CH_4,out}} \times 100\% \quad (3)$$

Where $F_{CH_4,in}$, $F_{CH_4,out}$ represent the molar flow rate of methane at inlet

Table 1
Summary of the properties of Pd-Pt catalysts.

Sample ID	Pd/Pt loading	Atomic Pd:Pt ratio	Treatment Temperature (℃)	Dispersion	Average particle diameter (nm)
Pd_1Pt_2	1 *wt.*% Pd, 3.67 *wt.*% Pt	1:2	C400-R650[&]	0.156	7.15
Pd_1Pt_1	1 *wt.*% Pd, 1.83 *wt.*% Pt	1:1	C400-R670	0.162	6.91
$Pd_1Pt_{0.5}$	1 *wt.*% Pd, 0.917 *wt.*% Pt	1:0.5	C400-R692	0.168	6.68
$Pd_1Pt_{0.15}$	1 *wt.*% Pd, 0.275 *wt.*% Pt	1:0.15	C400-R600	0.152	7.37
Monometallic Pd*	1 *wt.*% Pd	–	C430-R490	0.13	8.62
	1 *wt.*% Pd	–	C430-R530	0.11	10.18
	1 *wt.*% Pd	–	C430-R620	0.066	16.97
Monometallic Pt[#]	0.917 *wt.*% Pt	–	C450-R400	–	2.43
	0.458 *wt.*% Pt	–	C350-R350	–	1.37

Note: * : Dispersion was measured by O_2 volumetric chemisorption; #: Dispersion was measured by H_2 volumetric chemisorption; &: C denotes calcination, and R denotes reduction.

and outlet of the reactor, $F_{CO,out}$ and $F_{CO_2,out}$ the formation rate of CO and CO_2 measured at outlet of the reactor, S_{CO} and S_{CO_2} the selectivity of CO and CO_2, respectively.

Reaction kinetics was employed herein to analyze the surface active sites of bimetallic catalysts (Supplementary Information S4). Bimetallic catalysts possess not only alloy NPs, but also isolated Pt particles. The latter shows catalytic activity for methane oxidation even at very low oxygen pressure. Its catalytic performance was insensitivity to particle diameter, and the turnover rate was found to be constant in a small-particle diameter range [13,41]. Such a property was applied to separate surface Pd or Pt sites, see Supplementary Information S4. The turnover rate (r_{CH_4}) was defined as follows:

$$r_{CH_4} = \frac{x_{CH_4} \bullet F_{CH_4,in}}{n_{surf}} (0.003\% < x_{CH_4} < 3\%) \quad (4)$$

Where n_{surf} denoted surface active sites measured by chemisorption system. Apart from the measurement of conversion or selectivity, kinetics measurement should be conducted under differential condition. The conversion (x_{CH_4}) was controlled to be lower than 3% by diluting the catalysts with a dilution ratio of 1: 500 (m_{catalyst}: m_{SiC}).

2.3. Characterizations

HRTEM image and EDS mapping were observed via a Hitachi HD3000 TEM (210 kV), which was equipped with an aberration corrector that could offer a spatial resolution lower than 0.2 nm. Ethanol solution was used to disperse the catalyst sample by ultrasonic treatment for 10 min. Then several droplets of the mixed liquor were dropped onto a thin film, and dried for TEM observation. Temperature program reduction (Micromeritics, Auto-Chem II 2920) of the catalysts by CO was carried out in a fixed bed reactor with 8 mm inner diameter quartz reactor. The temperature was increased from 100 ℃ to 1000 ℃ at a heating rate of 2 ℃/min, and the feed gas with a total flow rate of 100 mL/min was composed of 1 kPa CO and Ar balance. After reaction, the outlet gas was directly fed into an online MS, by which the products of CO and CO_2 species were identified, and their proportions were estimated. The mass spectroscopy (MKS, Circle III-XD) could be directly linked to the outlet of the reactor, such as TPR, fixed bed reactor, reaction attachment of in situ FTIR, etc. Since its detection range varied from 0 to 200 g/mol, it could read CO, CO_2, CH_4, H_2, D_2, HD, etc., by continuously extracting small amount of outlet gas at the flow rate of 5×10^{-11} mol/min. Oven temperature was 180 ℃ for bakeout, and the temperature of ion source was 2000 ℃ (tungsten filament). This online MS was operated using Process Eye Professional software, which communicated with the system over a TCP/IP network.

The in situ XPS spectra was recorded in a Specs XPS chamber equipped with a MCD-10 analyzer and a monochromatic X-ray source of Al Kα. The catalyst powders with a mass of 100 mg was pressed onto a plate, and then loaded into XPS chamber. Before methane oxidation, all catalysts were reduced by hydrogen. Catalytic reactions were performed under different O_2/CH_4 ratio. After that, the chamber was degassed for 1 h for XPS measurement. XPS peak deconvolution was conducted by Peak-Fit 6.0 software. The full widths at half heights (FWHHs) and center locations of different species were referred to the published results [42,43].

The in situ XAS spectra of Pd-Pt bimetallic catalysts were collected at Pd K edge (24350 eV) at beamline 8-ID (IS, 10^{14} ph/s, 10 keV) and 8-BM (QA, 2×10^{12} ph/s, 10 keV) of the National Synchrotron Light Source in Beijing. For each in situ XAS measurement, 100 mg bimetallic sample was loaded into a copper cell. Reactor windows were sealed by two pieces of graphite carbon paper, and quartz wools were placed on both sides of catalyst bed. For each measurement, fresh catalysts were reduced firstly, and then exposed to the reaction atmosphere. In this research, XANES spectra were collected during the reaction, while EXAFS spectra were collected after catalytic oxidation with the evacuation of the reaction chamber for 1 h. XAS spectra were collected at a speed of 1 scan/min. The scanned spectra were merged with identical features as an individual spectrum to improve the ratio of signal to noise. Pd and Pt foils were employed here to be the standard references that calibrated energy shifts and calculated passive electron reduction factor. Results processing was performed by IFFEFIT package and EaVX code [44,45].

The in situ infrared spectroscopy were performed in a transmission attachment mounted in a Fourier transform infrared spectroscopy (PerkinElmer, FTIR, MCT detector, 0.2 cm^{-1} resolution). Pd-Pt catalysts were pressed into a wafer with ~1 cm diameter, and then loaded onto FTIR transmission attachment. For each experiment, the in situ catalytic oxidation was conducted at high temperature for 2 h. After the reaction, reaction chamber was degassed for 1 h, and then CO pulse was introduced to perform chemisorption at room temperature. During the measurement, the residual gas in the reactor was evacuated continually using a vacuum pump. CO was adsorbed on Pd-Pt surface active sites as a monolayer. IR spectra were collected in the wavenumber of 600 – 4200 cm^{-1} with the resolution of 0.1 cm^{-1}. The details about spectra deconvolution was shown in Supplementary Information.

3. Result and discussion

In this work, methane partial oxidation was conducted in a fixed bed reactor using bimetallic Pd-Pt catalysts. Surface chemistry of the catalysts and the generated reaction intermediates were characterized via "in situ" technique, such as FTIR, XPS and XAS. The change of surface oxygen concentration, vacancy, ionic/metallic surface sites, and coordination number of used catalysts were calculated. Based on these parameters, the relationship of surface species on catalysts to the product selectivity in methane partial oxidation was discussed.

3.1. Catalytic performance of Pd-Pt bimetallic catalysts in methane partial oxidation

Fig. 1a, b and c display the HRTEM-EDS mapping of core shell structural $Pd_1Pt_{0.5}$, Pd_1Pt_1, Pd_1Pt_2 bimetallic catalysts. Their corresponding HRTEM images are shown in Fig. S2. Two types of Pd-Pt particles are found in these images, namely large Pt-core@Pd-shell particle, and small isolated Pt particles (marked in yellow circles). Both of them show contribution to methane catalytic oxidation, but with varied catalytic reaction routes and products under different O_2/CH_4 ratio [13,27]. Fig. 1d illustrates the core shell structural particle and small isolated Pt particle in prepared Pt-Pd catalysts. Interestingly, the large Pt-core@Pd-shell particles in different Pt-Pd catalysts possess different diameters, while little difference (ca. 1–2 nm) was observed for the diameters of the small Pt particles.

The catalytic oxidation of methane was performed over Pt-Pd core shell structural catalysts in a fixed bed reactor in an oxygen deficient environment, containing 1 kPa CH_4, 0.5 kPa O_2 and Ar, and with increased reaction temperatures from 150 ℃ to 700 ℃. In Figs. 1e and 1f, the methane conversion and the selectivity towards CO and CO_2 at different reaction temperatures are shown, respectively. The reaction has been divided into two regions according to the products, namely the region with only CO_2 and the region with dual component product of CO_2 and CO. When the temperature is lower than 500 ℃, complete oxidative reaction conducts over the three Pd-Pt catalysts, with CO_2 as the only product and methane conversion lower than 25% (Fig. 1e). At 500 ℃, a low CO selectivity of around 5% was observed (Fig. 1f). In the temperature range of 500 ℃~700 ℃, both methane conversion and CO selectivity continually increase. CO becomes a major product in outlet gas. In addition, the distribution of carbon species are calculated, and the results are displayed in Fig. S3.

Supplementary Information S4 describes the normalization methodology for the calculation of surface Pt sites in different bimetallic Pd-Pt system, which employs reaction kinetics to normalize surface active

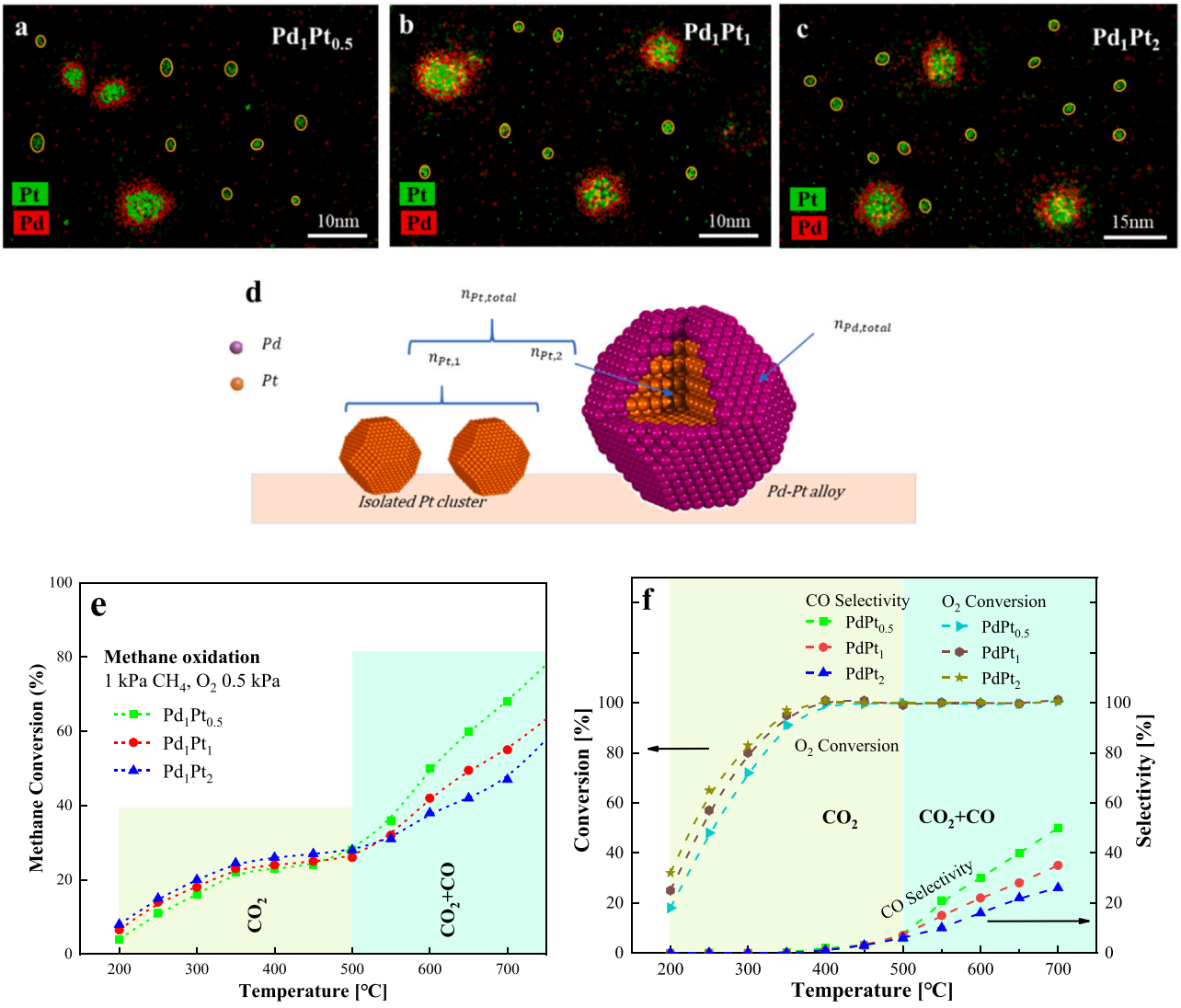

Fig. 1. HRTEM-EDS images of (***a***) $Pd_1Pt_{0.5}$, (***b***) Pd_1Pt_1, and (***c***) Pd_1Pt_2; (***d***) Schematic of Pt-core@Pd-shell structural catalyst; (***e***) Methane conversion as functions of reaction temperatures using different bimetallic Pd-Pt catalysts; (***f***) CO selectivity and O_2 conversion as functions of reaction temperatures using different bimetallic Pd-Pt catalysts (1 kPa CH_4, 0.5 kPa O_2).

sites. At low oxygen pressure of lower than 0.02 kPa, only Pt species play a role in catalytic reaction. Because diameters of isolated Pt particle in these bimetallic catalysts are around 1–2 nm, their catalytic reactivity is insensitive to particle diameter (Fig. S5a). Based on these reaction phenomena, exposed surface sites were compared and calculated (Fig. S5b), and the results are displayed in Table 2.

3.2. Core shell structural bimetallic catalyst without isolated Pt particles

Pt-core@Pd-shell structural catalyst with the absence of isolated Pt particles was established to avoid the consumption of CO over Pt species.

Table 2
Exposed surface active sites normalized by reaction kinetics.

Items	$Pd_1Pt_{0.5}$	Pd_1Pt_1	Pd_1Pt_2
$n_{surf\ total}$ (mol/g)	1.98741×10^{-5}	2.36798×10^{-5}	2.5935×10^{-5}
$n_{surf\ Pt,norm}$ (mol/g)	1.03622×10^{-5}	1.70356×10^{-5}	2.26028×10^{-5}
$n_{surf\ Pd,norm}$ (mol/g)	9.51187×10^{-6}	6.64417×10^{-6}	3.33221×10^{-6}
$n_{surf\ Pt,norm}$ / $n_{total,Pt}$ (%)	22.05%	18.13%	12.03%

Note: $n_{surfPd,norm} = n_{surf\ total} - n_{surfPt,norm}$.

Here, the Pt loading was decreased to a lower level, resulting in Pd: Pt atomic ratio of 1:0.15 ($Pd_1Pt_{0.15}$). In general, SiC support possesses lower specific surface area than other commonly used supports such as SiO_2, Al_2O_3, molecular sieve, CNTs, etc. In other words, SiC provides less anchor points for Pd and Pt NPs in form of alloy or isolated crystals. Decreasing of Pt loading promotes the combination of a large amount of Pt species with Pd species, forming alloy particle on support surface, rather than dispersed or isolated Pt NPs.

The structure of Pd1Pt0.15 catalyst was detected using HRTEM-EDS technique (Fig. 2a). Different from those of $Pd_1Pt_{0.5}$, Pd_1Pt_1, and Pd_1Pt_2 (Fig. 1 a, b, and c, respectively), only core shell structural NPs with Pt core (green color) and Pd shell (red color) are observed, without the presence of isolated small Pt NPs. Fig. 2b shows the diameter distribution of Pd-Pt NPs, which is mainly located in the range of 6 nm ~ 9 nm. The average diameter of $Pd_1Pt_{0.15}$ sample is 7.37 nm. Such small diameter of the catalyst is beneficial for methane oxidation. Fig. 2c and d depict the radial distribution of Pd and Pt species for two representative core shell structural Pd-Pt NPs shown in Fig. 2a. Obviously, in these core-shell NPs, the shell with Pd: (Pd+Pt) molar ratio higher than 90% is mainly composed of Pd species, while the core with Pt: (Pd+Pt) molar ratio of 64 − 72 mol.% is mainly composed of Pt species. A small proportion of Pd species still remains in the inner core of synthesized

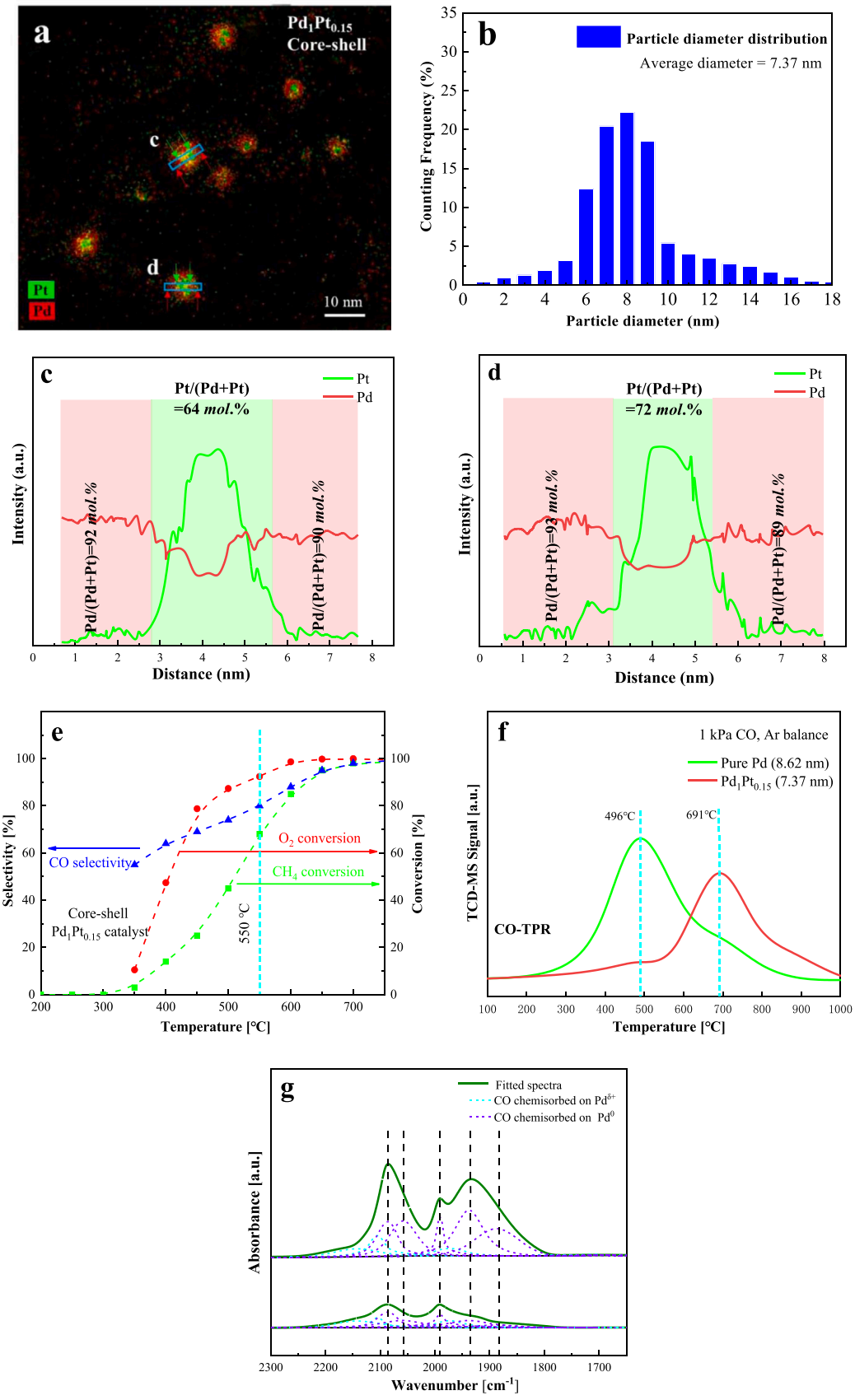

Fig. 2. **a**. HRTEM-EDS images of core shell structural $Pd_1Pt_{0.15}$ catalyst; **b**. Diameter distribution of $Pd_1Pt_{0.15}$ core shell NPs; **c** and **d**. Distribution of Pd and Pt species in typical NPs; **e**. Conversion and Selectivity as functions of reaction temperature in methane direct oxidation of $Pd_1Pt_{0.15}$ catalyst; **f.** Temperature programmed reduction of pure Pd and core shell $Pd_1Pt_{0.15}$ in oxidized state using CO (1 kPa CO, Ar balance); **g**. *In situ* FTIR spectra for observing CO species covered on the surface of core shell NPs (1 kPa CH_4, 0.5 kPa O_2, Ar balance, 550 ℃).

NPs. This is because most of Pt species migrate from shell to inner core, while not all Pd species migrate from core to shell.

Fig. 2e shows the CO selectivity and methane conversion as functions of reaction temperature from 200 ℃ to 700 ℃ using $Pd_1Pt_{0.15}$ catalyst. No conversion of methane is observed at temperature lower than 350 ℃, while sharp increases of methane conversion (from 0 to almost 100%) and CO selectivity (from 60 to nearly 100%) are obtained at temperature higher than 350 ℃. At 550 ℃, the methane conversion and CO selectivity reached the values of ~60% and ~80%, respectively, significantly higher than those obtained using $Pd_1Pt_{0.5}$, Pd_1Pt_1, or Pd_1Pt_2 samples. In addition, the carbon distribution during methane direct oxidation over $Pd_1Pt_{0.15}$ catalyst was also calculated and shown in Fig. S4.

Fig. 2f shows the temperature programmed reduction of oxidized mono-Pd sample and core shell structural $Pd_1Pt_{0.15}$ sample by CO (1 kPa CO in Ar balance). Before TPR, the monometallic Pd catalyst was oxidized at 550 ℃ for 5 h in the reaction gas containing 0.5 kPa O_2 and Ar. Then the oxidized sample was kept in Ar, and waited for CO reduction. The reduction peaks of mono-Pd and $Pd_1Pt_{0.15}$ are located at 496 ℃ and 691 ℃, respectively, indicating that oxygen species on $Pd_1Pt_{0.15}$ surface is harder to be removed. This property may contribute to a high CO selectivity. It is known that CO formed via the reaction of CH_x free radicals (CH*, CH_2 *, CH_3 *, etc.) with oxygen species might be dissociated from the surface as the product or further oxidized with surface oxygen species to CO_2. In case of a strong binding between oxygen species and the surface of core shell catalyst, the deep oxidation of CO will be blocked or deactivated. Since CH_x free radicals is very active over catalyst surface, the methane conversion will not be blocked by this strong binding.

Fig. 2g illustrates the in situ FTIR spectra for observing CO intermediates formed on catalyst surface. CO mainly covers the metallic Pd active sites, indicating that the surrounding oxygen species has been consumed during the reaction. Compared with mono-Pd catalyst, more CO species are formed and chemisorbed on the surface of core shell catalyst. Considering that core shell catalyst exhibits low concentration of surface oxygen, and the chemisorbed CO is then released as product, instead of further oxidizing to CO_2. We also perform the co-feed experiment by using $^{12}CH_4$ and ^{13}CO **in** Fig. S6, to demonstrate CO, as the intermediate, mainly forms on core shell nanoparticle surface. The value of CO selectivity is similar to that of conversion of CO oxidation, indicating the product CO_2 comes from CO.

Supplementary Information S6 displays the catalytic performance for $Pd_1Pt_{0.15}$ catalyst. As shown in Fig. S7, the slope of $Pd_1Pt_{0.15}$ sample is lower compared to those of other three bimetallic samples. Combined with Equation S2, the normalized surface sites are calculated and shown in Table 3. The percentage of surface Pt sites in total surface sites is very low of only 0.45%. This means, most of Pt species is migrated under oxygen titration into Pd crystals, forming the core of $Pd_1Pt_{0.15}$ NPs. It should be noted that, in the following discussions regarding the oxygen concentration, vacancy, quantity of $Pd^{\delta+}$, and the coordination number, the normalized Pd sites is used ($n_{surf\ Pd,norm}$).

To compare the activation ability of surface Pd sites of pure Pd catalyst and $Pd_1Pt_{0.15}$ catalyst, isotopic exchange experiment in the temperature range from 250 ℃ to 600 ℃ using CD_4 +H_2 gas flow (1 kPa CD_4, 1 kPa H_2, and Ar balance) was conducted. Before the experiment, the two catalysts were reduced at 700 ℃, followed by the evacuation of the reactor for 12 h to remove all the chemisorbed species. During the exchange experiment, D atoms, from methane, re-combine with H adatoms to form D_2 or HD molecule. The exit gas were continuously measured by an online MS to detect exchanged products, i.e. D_2 and HD species. In Fig. 3a, the total intensity of D_2 + HD over $Pd_1Pt_{0.15}$ is much higher than that over mono-Pd, suggesting the stronger binding or bonding abilities of surface sites on core shell structured catalysts with hydrocarbon. This phenomenon is attributed to Pd 3d core-level shift and coordination number.

Table 3
The normalized surface sites for core shell structural $Pd_1Pt_{0.15}$ sample.

Items	$Pd_1Pt_{0.15}$ core-shell
$n_{surf\ total}$ (mol/g)	1.64255×10^{-5}
$n_{surf\ Pt,norm}$ (mol/g)	7.42718×10^{-8}
$n_{surf\ Pd,norm}$ (mol/g)	1.63512×10^{-5}
$n_{surf\ Pt,norm}$ / $n_{total,Pt}$ (%)	0.53%
$n_{surf\ Pt,norm}$ / $n_{surf\ total}$ (%)	0.45%

Fig. 3b shows the in situ XANES spectra of Pd k-edge of mono-Pd and $Pd_1Pt_{0.15}$ during the isotopic exchange reaction. Two suppressed white line of pure Pd sample and $Pd_1Pt_{0.15}$ sample are displayed separately. It is noted that both the reduced mono-Pd sample and $Pd_1Pt_{0.15}$ sample exhibit a suppressed white line from 24330 to 24390 eV. The highest normalized intensity is observed on $Pd_1Pt_{0.15}$ under exchange reaction condition, an indicator of a polarization of surface Pd atoms due to coordination of adsorption group, such as CH_x free radicals. This statement is in good accordance with previous results published in literature that surface of core shell structural catalyst possesses high surface free energy and low coordination number, which prefers to bond with other species to achieve thermodynamic equilibrium [46,47].

3.3. Vacancy, oxygen concentration, and coordination number

Surface vacancy and oxygen concentration influence the catalytic performance (e.g., methane conversion, product selectivity) of methane reaction as well as coordination number of surface species. In general, vacancy and reaction intermediates co-exist over surface active sites. Efforts have been made to produce vacancy or defect on the surface during C-H bond activation for improved catalytic performance [48,49]. For oxidative reactions, oxygen vacancy is usually considered. This is because the sites without bonded oxygen species possess high surface energy and are easy to coordinate with other species to maintain thermodynamic equilibrium. This coordination promotes the dissociation and bond fracture of other species, such as methane, which is beneficial for subsequent reaction process. In addition, a high quantity of vacancies lead to reduced surface concentration of oxygen species, resulting in increased average distance among oxygen adatoms. This situation can increase CO selectivity but decrease methane conversion. Thus, a suitable ratio of vacancy/adatom is essential to achieve higher yield of CO species.

To investigate vacancy and oxygen concentration, an in situ reaction attachment mounted in XPS technique was employed to measure chemisorbed species in CH_4/O_2 atmosphere with varied O_2/CH_4 ratio from 0.25, 0.5–0.75. The detailed reaction procedure was shown in Fig. S8. The catalysts were reduced in hydrogen prior to the reaction. Note that, methane reaction and XPS measurement were not synchronized. XPS measurement was conducted in vacuum after reaction.

Fig. S9 shows the Pd 3d XPS spectra for bimetallic $Pd_1Pt_{0.15}$ and mono-Pd samples. The peaks recorded on $Pd_1Pt_{0.15}$ both shift slightly (0.9 and 1.3 eV, respectively) to higher binding energies compared to those of mono-Pd catalyst, indicating that the oxygen desorption or Pd-O bond fracture on $Pd_1Pt_{0.15}$ are more difficult, inhibiting complete oxidation of CO species.

Fig. 4a shows O 1 s spectra of the bimetallic catalyst under different reaction conditions. It can be deconvoluted into two peaks located at 532.0 eV and 530.2 eV, assigned to surface oxygen and lattice oxygen, respectively. It is obvious that the intensity of detected O 1 s signal increases with the increase of oxygen pressure. Fig. 4b displays the change of methane conversion and CO selectivity on bimetallic catalyst by varying the pressure. The lowest conversion but the highest CO selectivity was observed at the low oxygen pressure of 0.25 kPa.

In order to establish the correlation of XPS spectra intensity with the quantity of surface oxygen adatoms, three monometallic Pd catalysts with different particle diameters of 8.62 nm, 10.18 nm and 16.97 nm were prepared (Table 1). The amount of surface sites of small particle is higher than that of large particle. To clarify whether oxygen is only

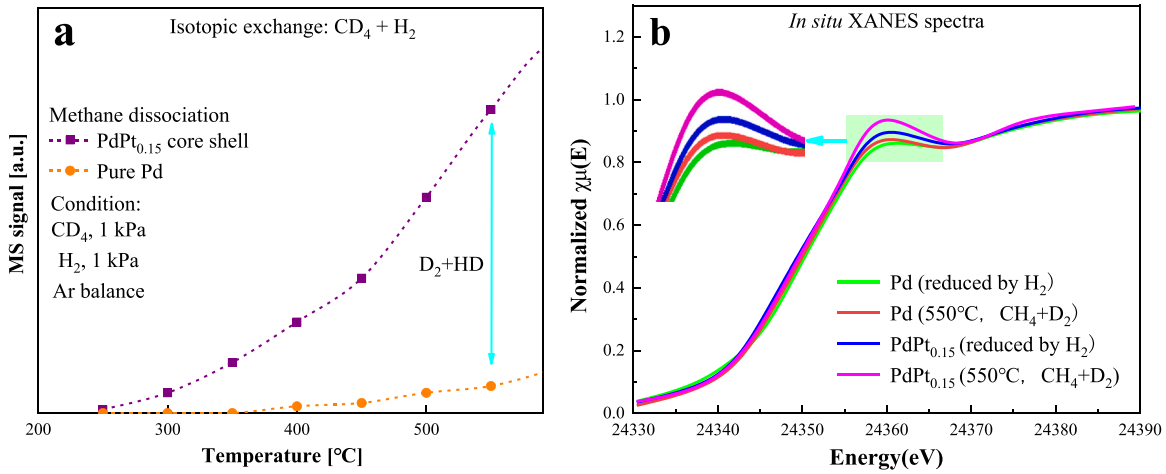

Fig. 3. a. Isotopic exchange experiment of CD_4 +H_2 over reduced mono-Pd (8.62 mn) and reduced $Pd_1Pt_{0.15}$ core shell (7.37 nm) sample (1 kPa CD_4, 1 kPa H_2); 3b. The in situ XANES spectra of Pd k-edge over mono-Pd and $Pd_1Pt_{0.15}$ core shell samples under different conditions (reduction by H_2 and isotopic exchange by CH_4/D_2).

chemisorption on Pd surface sites via monolayer adsorption with atomic ratio of Pd:O = 1:1, catalysts were pretreated by the procedure (Fig. S8) consisting of two step, namely hydrogen reduction and oxygen uptake. The former was performed at high temperature, while the latter at room temperature. Fig. 4c shows O 1 s XPS spectra of mono-Pd samples after oxygen monolayer chemisorption. It is obvious that lattice oxygen nearly disappears, and oxygen species are mainly chemisorbed over Pd crystal surface. In short, smaller particles with higher numbers of surface sites tend to attract more surface oxygen species, contributing to a higher XPS intensity.

Fig. 4d shows the linear correlation of the amounts of oxygen adatoms with the deconvoluted peak intensities at 532.0 eV for surface oxygen collected from the O1s XPS spectra in Fig. 4a and c. It employs monometallic Pd samples to establish the linear correlation, and calculate the quantity of oxygen adatoms by means of spectra intensity (see the red rectangle). Fig. 4e shows the variation of oxygen adatoms or vacancy as a function of O_2/CH_4 ratio. The summed number of vacancy and surface oxygen is equal to the number of surface Pd sites. In all cases, the quantity of oxygen adatoms are much lower than that of vacancy, leading to higher CO selectivity, but lower methane conversion. Table 4 summarizes the detailed parameters of surface species.

To further analyze the chemical state, i.e. ionic state or metallic state, of surface Pd species, in situ FTIR spectra were employed. Before measurement, the samples were treated via CO chemisorption at room temperature. Detailed treatment procedure is shown in Fig. S11. For the catalysts after methane reaction, the in situ FTIR was conducted after evacuation of the reaction chamber for 1 h to remove CH_x free radicals, surface hydroxyls, and other reversible adsorption species.

CO uptake is monolayer chemisorption with Pd: CO ratio of 1:1. Table S3 shows the assignments of IR absorption bands used for the deconvolution of spectra collected on Pd-Pt catalysts via CO chemisorption. The majority of adsorption configuration of CO over Pd and Pt surface are bridged adsorption and linear adsorption. Linear adsorption is the major configuration over Pt surface sites, while both bridged and linear adsorption play important roles for Pd surface sites. For linear adsorption, the ratio of Pd: CO is 1:1, while for bridged adsorption it is 2:1. This indicates, one CO molecule bridged adsorbed over two Pd sites, or one Pd site can coordinate two bridged adsorbed CO molecules. Therefore, total Pd: CO ratio is 1:1 either, and it can employ CO as probe molecule to evaluate surface Pd sites as well as their chemical state.

Fig. 5 shows FTIR spectra for core shell structural $Pd_1Pt_{0.15}$ catalyst performed by CO chemisorption. Before IR measurement, catalyst has performed methane direct oxidation at 550 ℃, and then is vacuumed for 1 h. After that, CO pulse was introduced into the in situ reaction cell to do CO chemisorption. The recorded IR spectra can be deconvoluted into different peaks (Fig. 5a) corresponding to different infrared absorption bands, in Table S3. Five absorption bands are included for metallic Pd^0 species (blue dash line in Fig. 5a), attributing to bridged adsorption at the wavenumber of 1881, 1940 and 1988 cm^{-1}, and linear adsorption at 2056 and 2080 cm^{-1}. As for ionic $Pd^{\delta+}$ species (red dash line in Fig. 5a), three infrared absorption bands assigned to bridged adsorption at the wavenumber of 1970 cm^{-1}, and linear adsorption at 2105 and 2145 cm^{-1} are shown. Full widths at half height (FWHH) are complied with the parameters in Table S3. The error of wavenumber is ± cm^{-1}.

Fig. 5b collects IR spectra intensity of $Pd^{\delta+}$ and Pd^{0+} species, and calculates quantity of surface $Pd^{\delta+}$ species based on the correlation of IR intensity vs. O_2/CH_4 ratio. Intensity assigned for $Pd^{\delta+}$ species have a slight increase with increasing O_2/CH_4 ratio. As for Pd^{0+} species, it shows a decreasing trend. Eq. (5) shows the calculation method for evaluating the quantity of surface $Pd^{\delta+}$ sites:

$$\frac{I_{Pd^{\delta+}}}{I_{Pd^0}+I_{Pd^{\delta+}}}=\frac{n_{Pd^{\delta+},surf}}{n_{Pd^0,surf}+n_{Pd^{\delta+},surf}}=\frac{n_{Pd^{\delta+},surf}}{n_{surf\,Pd,norm}} \quad (5)$$

Table 5 exhibits the calculation results of the quantity of surface $Pd^{\delta+}$ sites and Pd^0 sites with different reaction conditions. It reflects the oxidation of surface Pd sites, suggesting ionic $Pd^{\delta+}$ sites account for a lower percentage compared with metallic Pd^{0+} sites. Oxygen molecules adsorb and bond with surface Pd atoms firstly, and then are continuously consumed by methane to reach thermodynamic equilibrium. This equilibrium keeps a large number of surface Pd sites from being oxidized, especially at low oxygen pressure. N_{Pd-O} value indicates the coordination number of Pd-O shell. Low oxygen pressure demonstrates a low coordination number of Pd-O shell.

3.4. Stability and chemical bond

The segregation of Pd and Pt species was treated by active oxygen titration with O_3 pulse for ~80 h at 550 ℃. Unlike the oxidative environment applied for the synthesis of core shell structural catalyst, oxygen-deficient environment ($O_2/CH_4 < 2$) was used here to investigate the effect of oxygen species on the catalyst structure. Fig. 6a shows the change of methane conversion during 80 h methane oxidation in O_2/CH_4 gas flow (V_{O2}: V_{CH4} = 0.5) using different catalysts of $Pd_1Pt_{0.15}$ alloy, core shell structured $Pd_1Pt_{0.15}$, and mono-Pd. The core shell structural catalyst possesses the highest methane conversion of ca.70%, which remains almost unchanged during the lifetime test, revealing its high catalytic reactivity and stability. For Pd-Pt alloy and mono-Pd catalysts, significant decreases of methane conversion occur, indicating the deactivation of used catalysts.

After lifetime test, the used catalysts were evacuated by a pump for

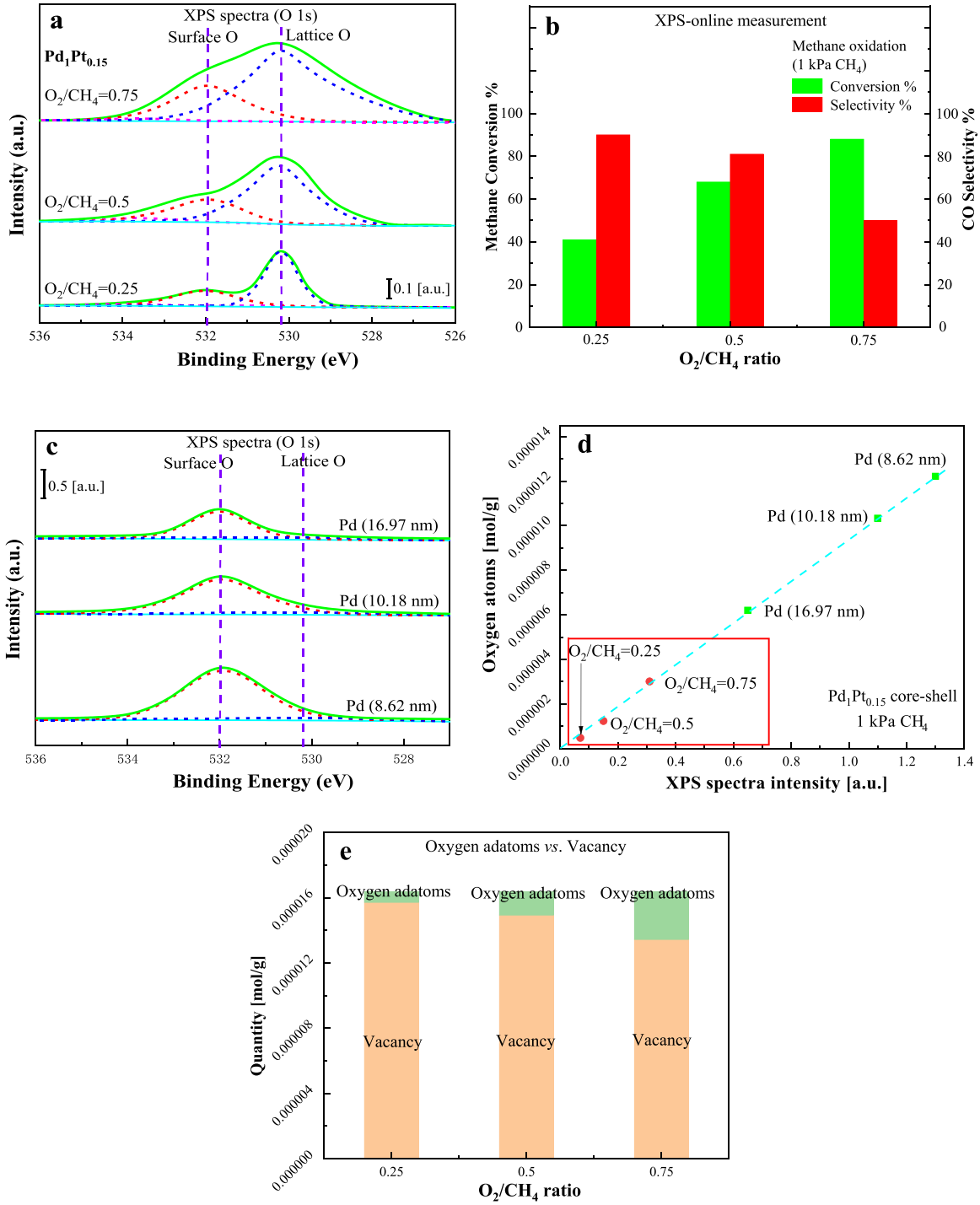

Fig. 4. XPS analysis for core shell structural $Pd_1Pt_{0.15}$ and mono-Pd catalysts. (**a**) O 1 s spectra of $Pd_1Pt_{0.15}$ sample under reaction conditions; (**b**) Conversion and selectivity of the reaction consequence of $Pd_1Pt_{0.15}$ sample via online measurement; (**c**) O 1 s spectra of mono-Pd samples by the treatment of oxygen monolayer chemisorption; (**d**) linear correlation of oxygen adatoms vs. XPS spectra intensity; (**e**) Quantity of oxygen adatoms/vacancy as a function of O_2/CH_4 ratio. (Reaction conditions are shown in Fig. S8 and Fig. S10).

2 h to remove reversible adsorption species, and then characterized using EXAFS measurement. XAFS spectra (Pd K edge) shown in Fig. 6b were collected at a speed of 1 scans/min. Two main peaks are observed and marked, assigned to the shell of Pd-O and Pd-Pd/Pt, respectively. The Pd-O shell is located in a small interval between 2.01Å and 2.20Å, while the Pd-Pd and Pd-Pt shell is located at 2.70Å. The inter-atomic distance for Pd-O shell varied slightly in different catalysts. The values were estimated to be 2.01, 2.14 and 2.20 Å for core shell, alloy and mono-Pd catalysts, respectively. Furthermore, FT magnitudes of core shell catalyst are higher than those of alloy and mono-Pd catalysts. As for Pd-Pd shell or Pd-Pt shell, the inter-atomic distances for the three samples are almost the same.

Table 6 summarizes EXAFS results of the three catalysts including coordination number (**C.N.**), distance (**R**), first nearest neighbor disorders (σ^2) and Cowley short range order. The distances of metallic bonds is constrained, namely $R_{Pd\text{-}Pt} = R_{Pt\text{-}Pd}$, to achieve better fitting of Pd K edge. The coordination number of Pd-O shell of core shell structured

Table 4
Surface parameters calculated by the correlation in Fig. 4**d**.

Item	Sample	Condition	$n_{surf\ Pd,norm}$ (mol/g)	I_{OIs} [a.u.]	$n_{surf\ O}$ (mol/g)	$n_{vacancy}$ [b] (mol/g)
Monolayer adsorption on Pd	Pure Pd (8.62 nm)	Monolayer adsorption (O)[a]	1.22157×10^{-5}	1.3	1.22157×10^{-5}	–
	Pure Pd (10.18 nm)	Monolayer adsorption (O)[a]	1.03364×10^{-5}	1.1	1.03364×10^{-5}	–
	Pure Pd (16.97 nm)	Monolayer adsorption (O)[a]	6.20184×10^{-6}	0.65	6.20184×10^{-6}	–
Reaction Condition	$Pd_1Pt_{0.15}$ core-shell	$O_2/CH_4 = 0.75$	1.63512×10^{-5}	0.31	2.91478×10^{-6}	1.34364×10^{-5}
	$Pd_1Pt_{0.15}$ core-shell	$O_2/CH_4 = 0.5$	1.63512×10^{-5}	0.15	1.41711×10^{-6}	1.49341×10^{-5}
	$Pd_1Pt_{0.15}$ core-shell	$O_2/CH_4 = 0.25$	1.63512×10^{-5}	0.07	6.3983×10^{-7}	1.57114×10^{-5}

Note: a. Oxygen adatoms uptake on surface Pd sites via monolayer adsorption;
b. $n_{vacancy} + n_{surfO} = n_{surfPd,norm}$;

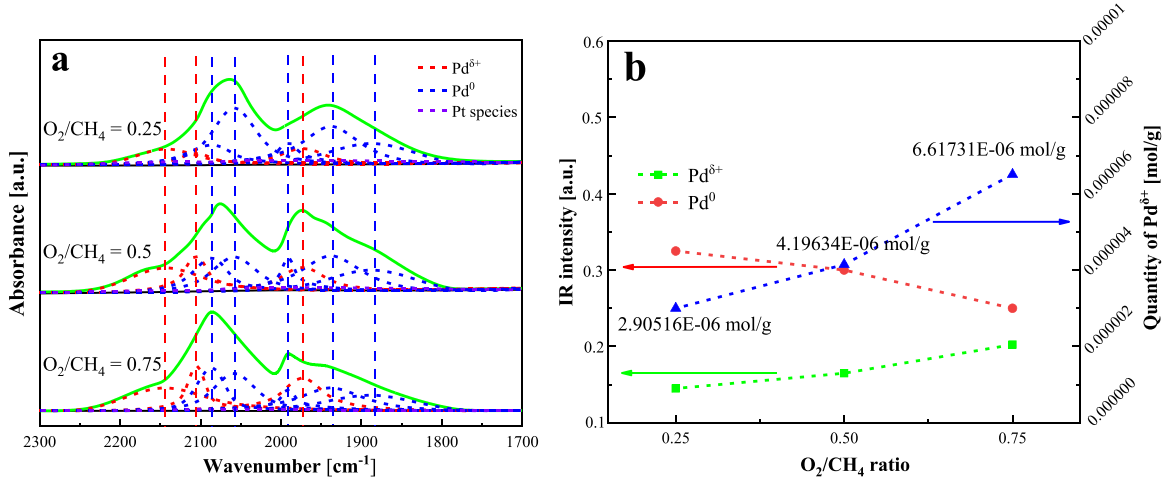

Fig. 5. *In situ* FTIR spectra for core shell structural $Pd_1Pt_{0.15}$ catalyst via CO chemisorption. (**a**) Spectra deconvolution for metallic and ionic Pd species by reaction conditions; (**b**) Correlation of IR intensity vs. O_2/CH_4 ratio, and their calculated results of quantity of ionic Pd species. (Methane oxidation: 1 kPa CH_4, O_2/CH_4 ratio of 0.25–0.75; CO uptake: CO pulse, room temperature).

Table 5
Quantity of surface $Pd^{\delta+}$ species as well as coordinated oxygen number for one Pd atom.

Catalyst ID	Condition	$\frac{I_{Pd^{\delta+}}}{I_{Pd^0}+I_{Pd^{\delta+}}}$	$n_{Pd^{\delta+},surf}$ [mol/g]	$n_{Pd^0,surf}$ [mol/g]	$n_{surf\ O}$ (mol/g)	N_{Pd-O}
$Pd_1Pt_{0.15}$	$O_2/CH_4 = 0.75$	0.123	2.0112×10^{-6}	1.434×10^{-5}	2.91478×10^{-6}	1.45
$Pd_1Pt_{0.15}$	$O_2/CH_4 = 0.5$	0.075	1.22634×10^{-6}	1.51249×10^{-5}	1.41711×10^{-6}	1.16
$Pd_1Pt_{0.15}$	$O_2/CH_4 = 0.25$	0.0512	8.37182×10^{-7}	1.5514×10^{-5}	6.3983×10^{-7}	0.76

Note: $N_{Pd-O} = n_{surfO}/n_{Pd^{\delta+},surf}$.

catalyst is lower than those of monometallic and alloy catalyst. Furthermore, the inter-atomic distance of core shell structured catalyst (2.01Å) is lower than those of mono-Pd and alloy samples, indicating a stronger combination between Pd and O in core shell structured catalyst, blocking further oxidation of CO to CO_2.

Cowley Parameters are calculated by coordination number and species composition in core shell structural NPs (Eq. 6) [50]:

$$\alpha = 1 - \frac{N_{AB}/N_T}{x_B} \quad (6)$$

Where N_{AB} and N_T denote the coordination number of A species and total coordination number, x_B denotes the molar percentage of B species which is characterized by EDS technique. Cowley short range parameter [50–52] is considered as an objective measurement to evaluate the short range order or species distribution in NPs. Cowley parameter of core shell catalyst is much higher than that of alloy sample, suggesting a regular arrangement or phrase of metal atoms that is caused by species segregation, the core shell structure. As for alloy catalyst, the distribution of Pd-Pt species possesses randomness, contributing to a lower Cowley parameter (0.42).

Fig. 6**c** shows the change of methane conversion as functions of reaction times during long-term methane catalytic oxidation with different O_2/CH_4 ratio using $Pd_1Pt_{0.15}$ core shell structured catalysts. The catalyst exhibits high stability with small or nearly unchanged methane conversion during 80 h reactions. The distribution of carbon species and the change of CO selectivity are provided in Fig. S12. With the increase of O_2/CH_4 ratio, the methane conversion increases, whereas the CO selectivity decreases. It can be seen that CO has the maximum production when $O_2/CH_4 = 0.5$. Though CO selectivity at $O_2/CH_4 = 0.25$ is highest, low methane conversion leads to a low CO production. CO selectivity is shown with to be suitably stable during 80 h reactions. The EXAFS spectra recorded on the catalysts collected after life time test are illustrated in Fig. 6d. The distances of Pd-O and Pd-Pd shell both maintain nearly constant with different O_2/CH_4 ratios. However, with decreased O_2/CH_4 ratio, the coordination number of Pd-O shell decreases from 0.64 to 1.10. This variation is in consistent with the results shown in Table 5 (N_{Pd-O}). XPS-IR (*Section 3.3*) is only aimed for the

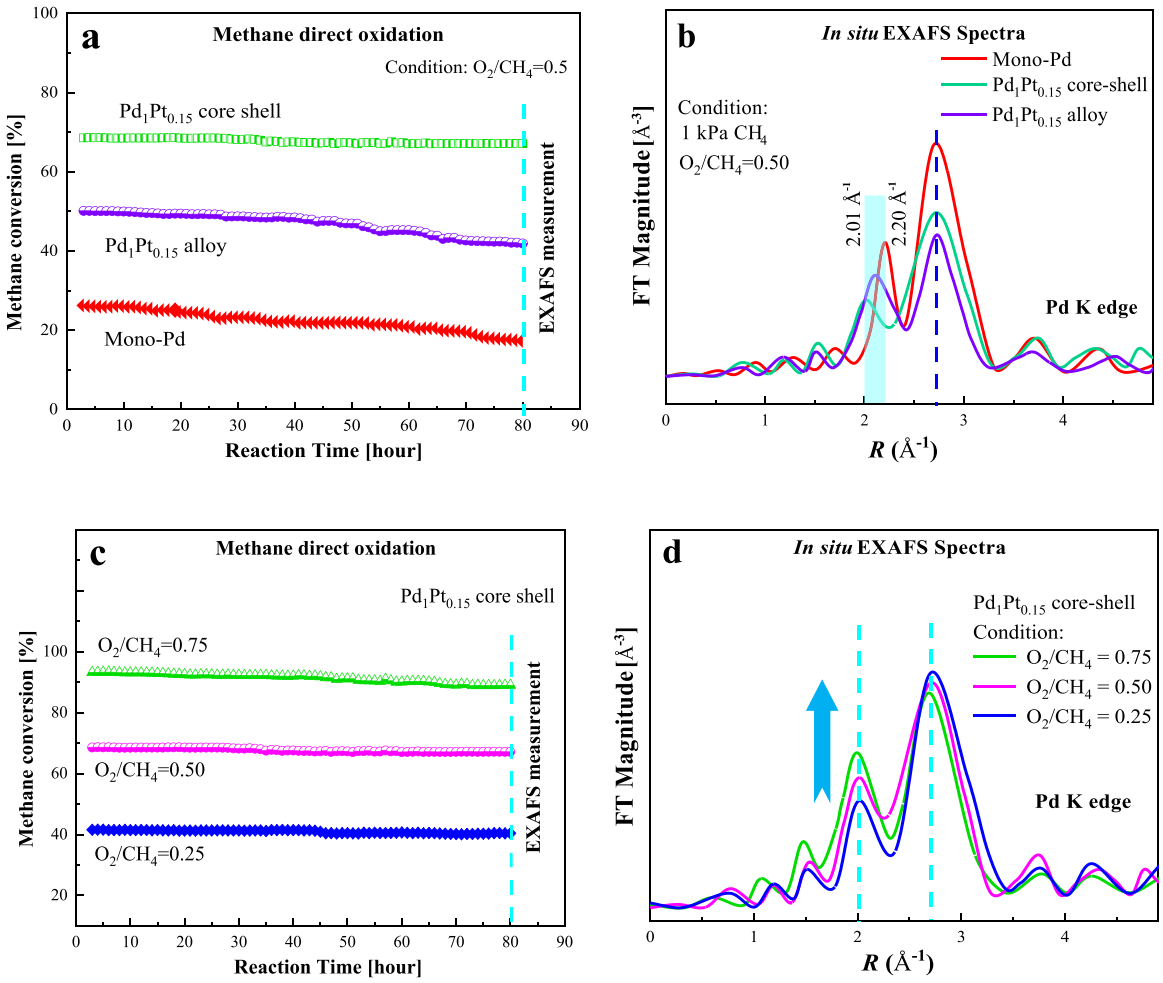

Fig. 6. *In situ* EXAFS experiment for Pd-Pt catalysts. (**a**) Stability of methane catalytic oxidation for $Pd_1Pt_{0.15}$ alloy, $Pd_1Pt_{0.15}$ core shell, and mono-Pd samples at O_2/CH_4 ratio of 0.5, 550 ℃; (**b**) The corresponding EXAFS spectra collected from **Figure a**, vacuum; (**c**) Stability of methane catalytic oxidation performed over $Pd_1Pt_{0.15}$ core-shell catalyst with different O_2/CH_4 ratio of 0.25, 0.5 and 0.75, 550 ℃; (**d**) The corresponding EXAFS spectra collected from **Figure c**, vacuum.

analysis of surface species, while EXAFS provides information of not only surface species, but also bulk phase species in the inner part of NPs. Nevertheless, the low coordination number or low coordination number in case of low oxygen pressure is beneficial for the improvement of CO selectivity.

In addition, the change of structure of $Pd_1Pt_{0.15}$ catalyst after the treatment under reaction condition of 700 ℃ for 50 h are also characterized by HRTEM-EDS and shown in Fig. S13. Almost no change is observed on the core shell structure after long-term reaction (Fig. S13a), whereas the average particle diameter is increased slightly from 7.37 to 7.78 nm (Fig. S13b), indicating the good stability of the catalyst.

In this paper, the effect of oxygen concentration, vacancy, coordination, distances, etc., on methane catalytic oxidation has been investigated. Their correlations to methane conversion and CO selectivity have been demonstrated. Since exposed Pt surface sites consume a large amount of CO for the formation of CO_2, the Pt loading was decreased to reduce surface Pt atoms significantly via migrating Pt species to bimetallic NPs as a core. This treatment results in core shell structural particle over support surface. Different from mono-Pd catalysts, exposed Pd sites over core shell structured catalysts can dissociate methane molecules to high reactive CH_x free radicals, which are able to react with surface oxygen with low concentration and strong coordination to form CO product. Further oxidation of CO is blocked under this chemical environment due to the strong combination. Higher oxygen concentration and coordination number lead to higher methane conversion, while more vacancy and lower coordination number result in higher CO selectivity.

4. Conclusion

This paper introduces a novelty core shell structural $Pd_1Pt_{0.15}$ catalyst that possesses a good catalytic performance in the conversion of methane to CO. Many “in situ” techniques are employed to characterize its surface properties, such as XPS, FTIR, XAS, etc. The conclusions are listed as below:

i) By decreasing Pt loading, the quantity of isolated Pt particles or surface Pt sites reduced significantly, suppressing the consumption of CO by surface oxygen species chemisorbed over exposed Pt sites.
ii) Core shell structural catalyst was very active to dissociate methane, contributing to a higher methane conversion than monometallic Pd sample.
iii) Lower oxygen pressure contributed to a lower concentration of surface oxygen, but more vacancy on surface. Higher number of vacancy led to increased CO selectivity.
iv) During methane catalytic oxidation, core shell structured catalysts possessed lower coordination number of Pd-O shell compared to mono-Pd sample, indicating stronger bonding of Pd-O, thus leading to blockage of the further oxidation of CO.

Table 6
Summary of EXAFS results for Pd-Pt catalysts under different reaction conditions.

Sample / Conditions	XAS edge	Shell	C.N.	R (Å)	σ^2 ($\times$ 0.01Å)	Cowley Parameter
Collected from Fig. 6b	$Pd_1Pt_{0.15}$ core-shell, $Pd_1Pt_{0.15}$ alloy and Mono-Pd (O_2/CH_4 =0.50)					
$Pd_1Pt_{0.15}$ core-shell	Pd K	Pd-O	0.82 (2)	2.01 (2)	0.46(6)	0.76
		Pd-Pd	2.6 (3)	2.70 (1)	0.61(3)	
		Pd-Pt	1.3 (5)	2.70 (1)	0.68(2)	
$Pd_1Pt_{0.15}$ alloy	Pd K	Pd-O	1.5 (2)	2.14 (1)	0.68(6)	0.42
		Pd-Pd	2.1 (3)	2.71 (1)	0.85(2)	
		Pd-Pt	0.8 (1)	2.70 (2)	0.77(4)	
Mono-Pd	Pd K	Pd-O	3.4 (2)	2.20 (2)	0.81(2)	–
		Pd-Pd	5.9 (6)	2.71 (2)	0.64(5)	
Collected from Fig. 6d	$Pd_1Pt_{0.15}$ core-shell catalyst with different O_2/CH_4 ratio					
O_2/CH_4 = 0.25	Pd K	Pd-O	0.64(3)	2.00 (4)	0.34(5)	0.71
		Pd-Pd	2.8(4)	2.70 (3)	0.45(2)	
		Pd-Pt	1.4(2)	2.70 (3)	0.59(3)	
O_2/CH_4 = 0.50	Pd K	Pd-O	0.82(2)	2.01 (2)	0.46(6)	0.76
		Pd-Pd	2.6(3)	2.70 (1)	0.61(3)	
		Pd-Pt	1.3(5)	2.70 (1)	0.68(2)	
O_2/CH_4 = 0.75	Pd K	Pd-O	1.10(3)	2.01 (7)	0.51(4)	0.82
		Pd-Pd	2.3(2)	2.70 (1)	0.67(8)	
		Pd-Pt	1.6(4)	2.70 (1)	0.72(1)	

CRediT authorship contribution statement

Haojie Geng: Conceptualization, Writing, Paper logic, Methodology, Investigation. **Haobo Zhao:** Writing, TPR, TEM-EDS experiments. **Siyu Yu:** Writing, XPS experiment, Catalytic activity evaluation. **Dongwei Li:** Visualization, Formal analysis, Discussion, Calculation. **Hong Lei:** EXAFS experiment and analysis. **Yuting Zhang:** Review, Supervision, Funding.

Declaration of Competing Interest

The authors declare that they have no known competing financial interests or personal relationships that could have appeared to influence the work reported in this paper.

Data Availability

Data will be made available on request.

Acknowledgements

This work was supported by the National Natural Science Foundation of China (22109129, 21905235) and Fundamental Research Funds for the Central Universities of China (SWU119003). We thank Professor Ya-Huei (Cathy) Chin for the help of kinetic research.

Appendix A. Supporting information

Supplementary data associated with this article can be found in the online version at doi:10.1016/j.apcatb.2022.122189.

References

[1] N. Agarwal, S.J. Freakley, R.U. McVicker, S.M. Althahban, N. Dimitratos, Q. He, D. J. Morgan, R.L. Jenkins, D.J. Willock, S.H. Taylor, C.J. Kiely, G.J. Hutchings, Aqueous Au-Pd colloids catalyze selective CH_4 oxidation to CH_3OH with O_2 under mild conditions, Science 358 (2017) 223–227.
[2] M.D. Marcinkowski, M.T. Darby, J. Liu, J.M. Wimble, F.R. Lucci, S. Lee, A. Michaelides, M. Flytzani-Stephanopoulos, M. Stamatakis, E.C.H. Sykes, Pt/Cu single-atom alloys as coke-resistant catalysts for efficient C–H activation, Nat. Chem. 10 (2018) 325–332.
[3] V.A. Kondratenko, U. Karimova, A.A. Kasimov, E.V. Kondratenko, Methane conversion into synthesis gas over supported well-defined Pt, Rh or Ru nanoparticles: effects of metal and support, Appl. Catal. A Gen. 619 (2021), 118143.
[4] B. Yza, H. Yu, C. Scl, D. Jjcab, The mechanism of room temperature catalytic C–H dissociation and oxygenation of formaldehyde over nano-zirconia phase-junction, Chem. Eng. J. 380 (2020), 122498-122498.
[5] M.C. Simons, S.D. Prinslow, M. Babucci, A.S. Hoffman, J. Hong, J.G. Vitillo, S. R. Bare, B.C. Gates, C.C. Lu, L. Gagliardi, A. Bhan, Beyond radical rebound: methane oxidation to methanol catalyzed by iron species in metal-organic framework nodes, J. Am. Chem. Soc. 143 (2021) 12165–12174.
[6] A. Andersen, F. Muntean, D. Walter, C. Rue, P.B. Armentrout, Collision-induced dissociation and theoretical studies of Mg^+ complexes with CO, CO_2, NH_3, CH_4, CH_3OH, and C_6H_6, J. Phys. Chem. A 104 (2000) 692–705.
[7] M. Tahir, B. Tahir, N. Amin, H. Alias, Selective photocatalytic reduction of CO_2 by H_2O/H_2 to CH_4 and CH_3OH over Cu-promoted In_2O_3/TiO_2 nanocatalyst, Appl. Surf. Sci. 389 (2016) 46–55.
[8] A.S. Nizovtsev, Activation of C-H bond in methane by Pd atom from the bonding evolution theory perspective, J. Comput. Chem. 34 (2013) 1917–1924.
[9] H. Geng, Z. Yang, L. Zhang, J. Ran, Y. Yan, M. Guo, Effects of O_2/CH_4 ratio on methane catalytic combustion over Cu/γ-Al_2O_3 particles, Int. J. Hydrog. Energy 41 (2016) 18282–18290.
[10] Z. Hou, L. Dai, J. Deng, G. Zhao, L. Jing, Y. Wang, X. Yu, R. Gao, X. Tian, H. Dai, D. Wang, Y. Liu, Electronically engineering water resistance in methane combustion with an atomically dispersed tungsten on PdO catalyst, Angew. Chem. Int Ed. Engl. (2022) e202201655.
[11] J. Shan, M. Li, L.F. Allard, S. Lee, M. Flytzani-Stephanopoulos, Mild oxidation of methane to methanol or acetic acid on supported isolated rhodium catalysts, Nature 551 (2017) 605–608.
[12] M. Jørgensen, H. Grönbeck, First-principles microkinetic modeling of methane oxidation over Pd(100) and Pd(111), ACS CATAL 6 (2016) 6730–6738.
[13] Y.H. Chin, C. Buda, M. Neurock, E. Iglesia, Reactivity of chemisorbed oxygen atoms and their catalytic consequences during CH_4-O_2 catalysis on supported Pt clusters, J. Am. Chem. Soc. 133 (2011) 15958–15978.
[14] A. An, A. Ms, B. As, B. Sjs, A. Hb, C. Bn, A comparative study of palladium-based coordination compounds with bidentate (N,N, P,P and P,O) ligands; design, synthesis, X-ray structural, catalytic activity and DFT studies, Inorg. Chim. Acta 515 (2020).
[15] H. Liao, M. Liu, P. Zuo, Preparation of Pd/$(Ce_{1-x}Y_x)O_2$ /γ-Al_2O_3 / cordierite catalysts and its catalytic combustion activity for methane, Catal. Commun. 76 (2016) 62–66.
[16] Y. Xu, X. Chen, Z. Wang, S. Fan, Y. Zheng, Effects of binary Co–Mn oxides promoters on low-temperature catalytic performance of Pd/Al_2O_3 for methane combustion, Int. J. Hydrog. Energy 46 (2021).
[17] Y. Gao, Y. Shen, Q. Zhu, J. Ma, H. Ren, Mechanisms and energetics of CO oxidation on MnO_2-supported Pt_{13} clusters, Appl. Surf. Sci. 560 (2021), 150017.
[18] J.S. Yoon, Y.-S. Lim, B.H. Choi, H.J. Hwang, Catalytic activity of perovskite-type doped $La_{0.08}Sr_{0.92}Ti_{1-x}M_xO_{3-\delta}$ (M = Mn, Fe, and Co) oxides for methane oxidation, Int. J. Hydrog. Energy 39 (2014) 7955–7962.
[19] P. Lott, M. Eck, D.E. Doronkin, A. Zimina, O. Deutschmann, Understanding sulfur poisoning of bimetallic Pd-Pt methane oxidation catalysts and their regeneration, Appl. Catal. B Environ. (2020), 119244.
[20] R.S. Kim, E.C. Wegener, M.C. Yang, M.E. O'Reilly, Y. Surendranath, Rapid electrochemical methane functionalization involves Pd–Pd bonded intermediates, J. Am. Chem. Soc. 142 (2020) 20631–20639.
[21] Y.Q. Su, I. Filot, J.X. Liu, E. Hensen, Stable Pd-doped ceria structures for CH_4 activation and CO oxidation, ACS Catal. 8 (2018) 75–80.
[22] Z. Chen, Q. Jiang, H. An, J. Zhang, S. Hao, X. Li, L. Cai, W. Yu, K. You, X. Zhu, C. Li, Platinum group metal catalyst (RuOx, PtOx, and IrOx)-decorated ceria-zirconia solid solution as high active oxygen carriers for solar thermochemical CO_2 splitting, ACS Catal. 12 (2022) 7719–7736.
[23] T. Ding, X. Liu, Z. Tao, T. Liu, T. Chen, W. Zhang, X. Shen, D. Liu, S. Wang, B. Pang, D. Wu, L. Cao, L. Wang, T. Liu, Y. Li, H. Sheng, M. Zhu, T. Yao, Atomically precise dinuclear site active toward electrocatalytic CO_2 reduction, J. Am. Chem. Soc. 143 (2021) 11317–11324.
[24] Z. Cheng, L. Qin, M. Guo, M. Xu, J.A. Fan, L.S. Fan, Oxygen vacancy promoted methane partial oxidation over iron oxide oxygen carriers in the chemical looping process, Phys. Chem. Chem. Phys. 18 (2016) 32418–32428.

[25] M.B.A.-S. Robert, L. McCormick, Gokhan O. Alptekin, Partial oxidation of methane, methanol, formaldehyde, and carbon monoxide over silica: global reaction kinetics, Appl. Catal. A Gen. 226 (2002) 129–138.
[26] H. Nassiri, R.E. Hayes, N. Semagina, Stability of Pd-Pt catalysts in low-temperature wet methane combustion: metal ratio and particle reconstruction, Chem. Eng. Sci. 186 (2018) 44–51.
[27] H. Geng, L. Zhang, Z. Yang, Y. Yan, J. Ran, Effect of Pd/Pt ratio on the reactivity of methane catalytic combustion in bimetallic Pd-Pt catalyst, Int. J. Hydrog. Energy 43 (2018) 11069–11078.
[28] M. Hou, X. Zhang, C. Fu, W. Cen, J. Chen, Effects of Pd/Pt bimetal supported by γ-Al_2O_3 surface on methane activation, Phys. Chem. Chem. Phys. 22 (2020) 4692–4698.
[29] A. Evm, A. Izi, A. Say, A. Vau, A. Ipp, A. Mak, B. Zria, Hydrogen production through autothermal reforming of CH_4: Efficiency and action mode of noble (M = Pt, Pd) and non-noble (M = Re, Mo, Sn) metal additives in the composition of Ni-M/$Ce_{0.5}Zr_{0.5}O_2$/Al_2O_3 catalysts - ScienceDirect, Int. J. Hydrog. Energy 45 (2020) 33352–33369.
[30] M.S.S. Khine, L. Chen, S. Zhang, J. Lin, S.P. Jiang, Syngas production by catalytic partial oxidation of methane over ($La_{0.7}A_{0.3}$)BO_3 (A = Ba, Ca, Mg, Sr, and B = Cr or Fe) perovskite oxides for portable fuel cell applications, Int. J. Hydrog. Energy 38 (2013) 13300–13308.
[31] M.D. Salazar-Villalpando, A.C. Miller, Catalytic partial oxidation of methane and isotopic oxygen exchange reactions over ^{18}O labeled Rh/Gadolinium doped ceria, Int. J. Hydrog. Energy 36 (2011) 3880–3885.
[32] W. Shan, M. Fleys, F. Lapicque, D. Swierczynski, A. Kiennemann, Y. Simon, P.-M. Marquaire, Syngas production from partial oxidation of methane over $Ce_{1-X}Ni_XO_Y$ catalysts prepared by complexation–combustion method, Appl. Catal. A Gen. 311 (2006) 24–33.
[33] H. Kolev, A. Naydenov, Y. Karakirova, D. Stoyanova, B. Tzaneva, On the development of active and stable Pd–Co/γ-Al_2O_3 catalyst for complete oxidation of methane, Chem. Eng. J. 266 (2015) 329–338.
[34] Vedyagin, A. Aleksey, Volodin, M. Alexander, Kenzhin, M. Roman, Mishakov, Effect of metal-metal and metal-support interaction on activity and stability of Pd-Rh/alumina in CO oxidation, Catal. Today (2017) 73–81.
[35] Y. Ma, S. Li, T. Zhang, Y.Y. Zhang, L. Jiang, Constructing of Pd(PdO)/Co_3O_4@SiO_2 core-shell structure for efficient low-temperature methane combustion, Nanoscale 13 (2021) 5026–5032.
[36] T. Wang, L.Y. Li, L.N. Chen, T. Sheng, L. Chen, Y.C. Wang, P. Zhang, Y.H. Hong, J. Ye, W.F. Lin, Q. Zhang, P. Zhang, G. Fu, N. Tian, S.G. Sun, Z.Y. Zhou, High CO-tolerant Ru-based catalysts by constructing an oxide blocking layer, J. Am. Chem. Soc. (2022).
[37] Y. Shi, F. Zhang, Low-temperature pseudomorphic transformation of ordered hierarchical macro-mesoporous SiO_2/C Nanocomposite to SiC via Magnesiothermic Reduction, J. Am. Chem. Soc. 132 (2010) 5552–5553.
[38] Z. Saeedifar, A.A. Nourbakhsh, R.J. Kalbasi, E. Karamian, Low-temperature magnesiothermic synthesis of mesoporous silicon carbide from an MCM-48/polyacrylamide nanocomposite precursor, J. Mater. Sci. Technol. 29 (2013) 255–260.
[39] B. Zhao, H. Zhang, H. Tao, Z. Tan, Z. Jiao, M. Wu, Low temperature synthesis of mesoporous silicon carbide via magnesiothermic reduction, Mater. Lett. 65 (2011) 1552–1555.
[40] H. Geng, Z. Li, D. Li, H. Zhang, X. Wu, L. Zhang, O_3 titration for synthesis of Pt-Pd core-shell structural catalyst and its catalytic performance on C-H bond activation, Appl. Catal. A: Gen. 631 (2022), 118487.
[41] W. Tu, Y.-H. Chin, Catalytic consequences of the identity and coverages of reactive intermediates during methanol partial oxidation on Pt clusters, J. Catal. 313 (2014) 55–69.
[42] T. Odoom-Wubah, Z. Li, Z. Lin, T. Tang, D. Sun, J. Huang, Q. Li, Ascorbic acid assisted bio-synthesis of Pd-Pt nanoflowers with enhanced electrochemical properties, Electrochim. Acta 228 (2017) 474–482.
[43] Y. Qiao, N. Said, M. Rauser, Y. Kai, Q. Fei, N. Theyssen, W. Leitner, Preparation of SBA–15 supported Pt/Pd bimetallic nano–catalysts using supercritical fluid reactive deposition and their application in hydrogenation of levulinic acid to γ–valerolactone: how do solvent effects during material synthesis affect cataly, Green. Chem. 19 (2016) 977–986.
[44] J. Timoshenko, A. Kuzmi, J. Purans, EXAFS study of hydrogen intercalation into ReO_3 using the evolutionary algorithm, J. Phys.: Condens. Matter 26 (2014), 055401 - 055401.
[45] B. Ravel, M. Newville, ATHENA, ARTEMIS, HEPHAESTUS: data analysis for X-ray absorption spectroscopy using IFEFFIT, J. Synchrotron Radiat. 12 (2010).
[46] Z. Xie, X. Wang, X. Chen, P. Liu, J.G. Chen, General descriptors for CO_2-assisted selective C-H/C-C bond scission in ethane, J. Am. Chem. Soc. 144 (2022) 4186–4195.
[47] L. Chen, P. Verma, K. Hou, Z. Qi, S. Zhang, Y.S. Liu, J. Guo, V. Stavila, M. D. Allendorf, L. Zheng, M. Salmeron, D. Prendergast, G.A. Somorjai, J. Su, Reversible dehydrogenation and rehydrogenation of cyclohexane and methylcyclohexane by single-site platinum catalyst, Nat. Commun. 13 (2022) 1–9.
[48] K.J. Warren, J.R. Scheffe, The role of surface oxygen vacancy concentration on the dissociation of methane over nonstoichiometric ceria, J. Phys. Chem. C. (2019).
[49] C. Zhuo, Q. Lang, M. Guo, M. Xu, L.S. Fan, Oxygen vacancy promoted methane partial oxidation over iron oxide oxygen carriers in the chemical looping process, Phys. Chem. Chem. Phys. 18 (2016) 32418.
[50] A.I. Frenkel, Q. Wang, S.I. Sanchez, M.W. Small, R.G. Nuzzo, Short range order in bimetallic nanoalloys: an extended X-ray absorption fine structure study, J. Chem. Phys. 138 (2013), 064202.
[51] M.V. Castegnaro, W.J. Paschoalino, M.R. Fernandes, B. Balke, M.A. MC, E. A. Ticianelli, J. Morais, Pd-M/C (M = Pd, Cu, Pt) electrocatalysts for oxygen reduction reaction in alkaline medium: correlating the electronic structure with activity, Langmuir 33 (2017) 2734–2743.
[52] Q. Zhang, X. Peng, Y. Nie, Q. Zheng, J. Shangguan, C. Zhu, K.C. Bustillo, P. Ercius, L. Wang, D.T. Limmer, H. Zheng, Defect-mediated ripening of core-shell nanostructures, Nat. Commun. 13 (2022) 2211.